Tidal Stream Energy Site Assessment via Three-Dimensional Model and Measurements

Paul A. Work[1]*, Kevin A. Haas[1], Zafer Defne[2], Thomas Gay[3]

[1]*School of Civil and Environmental Engineering, Georgia Institute of Technology, 210 Technology Circle, Savannah, GA 31407-3039 USA*

[2]*U.S. Geological Survey, Woods Hole, MA USA*

[3]*South Carolina Department of Transportation*

Abstract

A methodology for assessment of the potential impacts of extraction of energy associated with astronomical tides is described and applied to a site on the Beaufort River in coastal South Carolina, U.S.A. Despite its name, the site features negligible freshwater inputs; like many in the region, it is a tidal estuary that resembles a river. A three-dimensional, numerical, hydrodynamic model was applied for a period exceeding a lunar month, allowing quantification of harmonic constituents of water level and velocity, and comparison to values derived from measurements, recorded at a location within the model domain. The measurement campaign included surveys of bathymetry and velocity fields during ebb and flood portions of a tidal cycle for model validation. Potential far-field impacts of a generic tidal energy conversion device were simulated by introducing an additional drag force in the model to enhance dissipation, resulting in 10-60% dissipation of the pre-existing kinetic power within a flow cross-section. The model reveals effects of the dissipation on water levels and velocities in adjacent areas, which are relatively small even at the 60% dissipation level. A method is presented to estimate the optimal vertical location for the energy conversion device and the potential power sacrificed by moving to a different altitude.

Keywords: Tidal power, hydrodynamic impact, hydrodynamic numerical model, acoustic Doppler current profiler, Parris Island, Beaufort River, South Carolina

1. Introduction

Tidally forced flows represent a very appealing source of renewable energy. Many major population centers border or straddle tidal rivers and estuaries, and the flows, while time-dependent, are more predictable than solar, wind, and wave resources. Although biofouling and corrosion are typically more significant concerns than for terrestrial alternatives such as wind power, the much greater density of water allows for viable energy harvesting at much lower flow speeds, given that power grows with the cube of flow speed. Even sites with nominally small tidal ranges may feature locally constricted flows that yield speeds suitable for energy extraction. And as improvements in efficiency and reductions in hardware cost develop, the critical flow speed for viable energy production will drop, increasing the number of exploitable sites.

Tidal power has been harnessed for production of electricity for decades (the tidal barrage at La Rance in France was built in the 1960's, for example), but the field can still be considered as being in its infancy, with few projects actually constructed to date. A barrage or dam will have different environmental impacts than a network of turbines at the same site; here the focus is on this latter scenario, often preferred for water quality, other environmental, and logistical concerns.

Water levels and flows forced by tides are typically represented by linear superposition of sinusoidal components (i.e. a Fourier series) with different frequencies, amplitudes, and phases. Analytical solutions or one-dimensional numerical models for flow within a simplified domain can shed light on the problem (e.g. Bryden and Melville [1], Blanchfield et al. [2], Garrett and Cummins [3], Atwater and Lawrence [4], Polagye and Malte [5]), but many of the processes and parameters that must be considered or included for site selection are nonlinear, and problem geometry is typically quite variable and complex. As a result, it is generally infeasible to make use of analytical solutions for any but the simplest problems or geometries, or perhaps for first-order screening of sites. Numerical modeling tools are an obvious choice for use in the site selection

*Corresponding author, 1-912-966-7943

Email addresses: paul.work@gatech.edu (Paul A. Work[1]), kevin.haas@gatech.edu (Kevin A. Haas[1]), zafer.defne@gatech.edu (Zafer Defne[2])

process, but some ground-truthing is also required to validate model results and detect other characteristics of a site that might not be revealed by hydrodynamic model results.

Many site assessment investigations have been performed, typically with a focus on power potential and the hydrodynamic implications of energy harvesting (e.g. Alnaser [6], Blunden and Bahaj [7], Brooks [8], Sutherland et al. [9], Blanchfield et al. [10], Karsten et al. [11], Polagye et al. [12], Carballo et al. [13], Tontolo et al. [14], Xia et al. [15], Brooks [16], Defne et al. [17], Defne et al. [18]). Methodologies for assessing sites are still in development. Most studies have focused on far-field hydrodynamics, with the energy harvesting system represented by an energy (or power) sink in the model. In this way the results can be assumed independent of many details of the device by which energy is harvested. One-, two-, and three-dimensional numerical models of hydrodynamics have all been employed. Wind, water density gradients, and wave forcing have typically not been included when describing flows; in some cases, flows have also been assumed steady. River inputs are also often neglected. The most frequent result that is cited is the annual power available at the site. The number of previous efforts that have included field data collection specifically for power potential assessment or model validation is surprisingly low.

As noted by Couch and Bryden [19], Garrett and Cummins [20] and Vennell [21], peak flow speed by itself (or the corresponding peak kinetic energy) is not a good measure of site potential; nor is tidal range. High peak flow speed does indicate large pre-development, peak kinetic energy, but energy extraction will modify the flow field and the extracted energy will not match the pre-development, peak kinetic energy. As discussed by Garrett and Cummins ([3], [20]), system efficiency will vary with the type, number, and arrangement of devices, and the size of the device or array relative to the channel cross-section. The extraction of kinetic energy from a flow with a free surface, as considered here, leads to a transfer of potential energy to kinetic form, some of which then also becomes available for extraction.

In addition to available power, many other factors should also be considered for site selection: proximity to consumption sites, available infrastructure, impacts on waterway navigability, avail-

able depth and cross-section size, potential for scour and changes in sedimentation patterns (Neill et al. [22], Defne et al. [17], Neill et al. [23]), and environmental impacts, among other factors. Here, the focus is on power potential and far-field fluid mechanics effects of power extraction.

Many of the sites investigated to date are in Europe; within North America, the Bay of Fundy, British Columbia and Alaska have received the most attention. The southeastern United States has received little attention in this regard, because of smaller tidal ranges. Defne et al. [18] describe the tidal power potential throughout the U.S. state of Georgia, representing part of a larger effort to quantify tidal power potential for the entire U.S. via hydrodynamic model results. The Georgia Bight features the largest tidal range within the southeastern U.S., and many sinuous rivers (estuaries) that in some locations lead to potentially suitable flows for extraction of tidal power.

Here a combined effort involving both numerical modeling and field measurements is described, focusing on a site on the Beaufort River in South Carolina, USA, at the U.S. Marine Corps Recruit Depot at Parris Island. The site features negligible freshwater inputs, and negligible variation in salinity through a tidal cycle. Field measurements were used to validate results from a three-dimensional numerical model of tidally forced hydrodynamics. In addition to site-specific results defining the potential for power production at the site, the overall strategy for assessment of site suitability based on hydrodynamic characteristics and the optimization of the vertical location of energy harvesting equipment within the water column are also addressed.

2. Site Description and Field Measurements

The site that was the focus of the investigation is situated between the confluence of the Broad and Beaufort Rivers in coastal South Carolina, USA (Figure 1). These rivers are tidally dominated, and feature relatively large tidal ranges for the southeastern United States, with mean and diurnal ranges of 2.3 and 2.5 meters, respectively. The Parris Island Marine Corps Recruit Depot already has much of the necessary land-based infrastructure in place to receive renewable power, and a deeper section of the Beaufort River abuts the eastern side of Parris Island, making it a good

candidate site. It is roughly 15 km upstream of the entrance to Port Royal Sound, and as a result is sheltered from ocean wave energy, although some locally generated wind wave energy exists at times. The site lies between the Intracoastal Waterway and Parris Island, and the area features extensive tidal marshes, mudflats and oyster beds.

A field measurement campaign was designed with three goals: 1) acquire bathymetric survey data, 2) measure spatial (and to some degree, temporal) variations in ebb and flood flow fields, and 3) document longer-term (lunar month) variability in tidal characteristics at a promising location. Each component of the field investigation is considered below.

2.1. Bathymetric Survey

The survey was performed in one day from a small boat, using a 200 kHz acoustic depth-sounder and a pair of survey-grade, dual-frequency GPS receivers, one deployed as a fixed base station and the other on the boat. The boat followed a pre-defined track with survey transects roughly 250 m apart. The data were sampled at 5 Hz, resulting in decimeter-level horizontal resolution along the boat survey track. The larger scale bathymetric grid shown in Figure 1 was derived from U.S. National Ocean Service data for the numerical modeling discussed below. The new survey provided higher-resolution data to investigate site suitability in terms of water depth, and to show that the larger bathymetric dataset (based on an assimilation of many years of data) provided a reasonable depiction of site bathymetry. Compared to most potential tidal power extraction sites described previously by other investigators, the Beaufort River site is quite shallow (<10 m), but one option being considered is the deployment of a turbine suspended from a floating barge, which could be feasible for modest turbine sizes.

2.2. Roving Velocity Measurements

A 1200 kHz acoustic Doppler current profiler (ADCP) equipped with bottom-tracking firmware was deployed in down-looking mode from the bow of the survey vessel as it transited the area for the bathymetric survey. The instrument acquired data at 2 Hz with the velocity profile measured

with 0.5 m vertical resolution from a point 0.75 m below the water surface down to the riverbed. Estimated speed uncertainty in the measurements with this configuration is ±6 cm/s.

The measurements were taken on a day which was roughly halfway between the spring and neap portions of the tidal cycle. The tidal cycle during which the measurements were taken was the larger of the two on that day and featured a range of 2.2 m, i.e. close to the mean range for the site. Data were acquired over a 2.5-hr window bracketing the flood tide, and then another 2.5-hr window bracketing the ebb portion of the tidal cycle. Flow speeds reached 0.9 m/s during the flood portion of the cycle, and 1.1 m/s during the ebb (Figure 2).

2.3. Stationary Velocity Measurements

After reviewing the velocity and depth data from the roving survey, a location was chosen for deployment of the same ADCP on the riverbed for longer-term, stationary measurements of water level and mean flows. The instrument was deployed in a bottom-mounted frame for 37 days at the location shown by the × in Figure 2. It was programmed to sample velocities at 1 Hz for three minutes out of every fifteen, yielding four mean velocity profile measurements per hour, with 0.5 m resolution over the vertical. After recovery, all acquired data passed standard quality tests.

Measurements from the standalone ADCP deployment were used to determine the tidal constituents of both the water level and currents via harmonic component analysis Pawlowicz et al. [24]. The tidal constituents and their effect on the water level at a particular location are represented by the series

$$\eta(t) = \sum_{i=1}^{I} a_i \cos(\omega_i t + \phi_i) \tag{1}$$

where $\eta(t)$ is the mean water level at time t, in this case measured using a pressure sensor integrated into the bottom-mounted ADCP; i and I represent the ith constituent and total number of constituents, respectively, and a_i, ω_i and ϕ_i are the amplitude, angular frequency and phase angle of the ith constituent, respectively. Tidal constituents of the velocity time series can be computed

using a similar approach which utilizes complex amplitudes to resolve the flow direction. These constituents may be used to produce predictions of tidal stage or velocity for any subsequent period of time. The new dataset revealed that both the water level and velocity are dominated by the M2 tidal constituent (primary lunar semi-diurnal constituent, period of 12.42 hrs), which represented more than half of each time series (Table 1). The time series are thus strongly semi-diurnal; the Formzhal number $F = (K_1 + O_1)/(M_2 + S_2)$ is 0.19 for the site. Time series generated using the harmonic analysis results provided a good estimate of the measured conditions: mean of the magnitude of the difference in water levels and flow speeds were 0.1 m and 5 cm/s, respectively, corresponding to 5% of measured maximum values (Figure 3).

The M4 and M6 "overtides", which reflect tidal wave asymmetry which tends to increase as depth decreases, were small (<10% of the M2 constituent) in both time series. Since flow-induced forces depend not only on flow speed but also on flow acceleration, it is important to realistically describe the actual shape of the velocity time series, as opposed to only the maximum magnitude. For this, all significant tidal constituents must be considered.

The measurements also revealed the insignificance of freshwater inputs at the site. Time- and depth-averaged flow speed for the 37-day measurement period was 2.5 cm/s, in the seaward direction, two orders of magnitude less than peak tidal flows. Independent measurements of surface salinity obtained during a tidal cycle were nearly constant, varying from 34.1 to 34.4 PSU.

The vertical variation in the mean flow can also be an important consideration for energy harvesting, as vertical gradients in flow speed imply vertical gradients in horizontal forces. In addition to influencing the overall net force and overturning moment on any submerged equipment, vertical force gradients can impose undesirable stresses on bearings, particularly for axial flow equipment. Figure 4 shows measured velocity profiles for maximum ebb and flood (each averaged over multiple three-hour windows including the maximum flow) and the mean magnitude vs. depth. The significance of the shear increases with surface flow speed, since there is a no-flow boundary at the bottom (which does not appear in the figure because of a near-bed/near-instrument zone in which

measurements are not possible). The mean ebb and flood profiles differ at this site, revealing the tidal asymmetry, but the seaward and landward fluxes are very nearly balanced.

3. Numerical Modeling of Tidal Currents

Tidal flows were also simulated numerically, with the field measurements described above used for validation. The Regional Ocean Modeling System (ROMS) was used for the simulations. ROMS is a three-dimensional, free-surface, terrain-following, numerical model which solves the Reynolds-averaged Navier-Stokes equations using the hydrostatic and Boussinesq approximations. Transport equations are used to solve momentum and scalar advection and diffusive processes, and an equation of state determines the density field accounting for temperature, salinity, and suspended sediment concentration (Haidvogel et al. [25]; Shchepetkin and McWilliams [26]). The model was used to simulate flows for the same 37-day period during which field measurements were made, with density and temperature both assumed constant in space and time, consistent with the field observations. Results from the model allow for a better definition of spatial variations in the flows within the study area and optimization of equipment siting. Additionally, the model can be used to simulate the effects of energy extraction on the estuarine hydrodynamics.

A 202 by 212 cell computational mesh was used in the model calculations, with the extent of the domain shown in the right panel of Figure 1. Resolution was 200 m by 200 m horizontally (similar to that employed to define the roving survey track line offsets), and eight layers in the vertical. Since the model is terrain-following, layer thickness varies with depth across the domain.

The ADCIRC tidal database for the western North Atlantic Ocean (Mukai et al. [27]) was used to define required tidal constituents on the seaward boundary of the ROMS model grid. The M2, S2, N2, K2, O1, K1, M4, M6, and Q1 components were included. Wind and wind wave forcing were not included.

The first two days of the model results were discarded to minimize the influence of model spin-up effects. Model results for water level, velocity, and the corresponding tidal constituents

derived from time series of each were compared to values derived from measurements to assess the need for model calibration. Parameters affecting wetland wetting and drying, bottom friction, and the time step used in model calculations were adjusted until the model results most closely resembled measurements. Ultimately a 30-second time step was used for the simulations. Differences between the ROMS model results and the measurements were similar in magnitude to the differences between the measured time series and those reconstructed using harmonic analysis results as discussed earlier. Mean, depth-averaged flow speeds reported by the model for the measurement location were about 10% (6 cm/s) less than in the measurements after calibration. Tidal constituents derived from the model results for both water level and velocity are compared to those derived from the measurements in Table 2.

Figure 5 shows the mean and maximum velocity fields predicted by the ROMS model. There is a location downstream of the region surveyed that features notably stronger flows that would have gone unrecognized without the model results. With the model calibrated, it was then possible to simulate energy extraction to predict changes in both water levels and flows that could potentially have detrimental influence on the environment, navigation, or sedimentation.

4. Simulation of Tidal Power Extraction

Removing power from any tidal flow will alter both the near-field and far-field flow patterns, to a certain degree. Reducing the kinetic power of the flow will introduce velocity gradients that enhance turbulence, dissipating energy, and also lead to transformation of potential energy to kinetic energy. The severity of these combined effects depends on the amount of power removed from the original, undisturbed flow, and the extracted power will depend on many factors, including the number and type of devices, their locations and sizes, and the fraction of the channel in which they are deployed. Some investigators have suggested that the total amount of dissipation caused by the power converters should be limited to 15-30 percent of the kinetic power contained in the existing flow (Bryden and Melville [1]; Couch and Bryden [19]; Hagerman et al. [28]; Polagye

et al. [29]). Here two scenarios lying on either side of this range are considered. Once the ROMS model was found to have recreated the in-situ current measurements to a reasonable degree, it was used to simulate the impact of the dissipation of power due to the placement of extraction devices near the ADCP deployment site.

A momentum sink is generally introduced into the governing momentum equations to simulate the energy extraction process (Bryden and Melville [1]; Garrett and Cummins [30]; Bryden et al. [31]). This method was implemented in this study using the ROMS model. Two separate cases are considered in which nominally 10 percent and 60 percent of the total kinetic energy contained in the channel cross-section at the in-situ ADCP deployment location is dissipated by the extraction devices. Emphasis is placed on the far-field effects, as local (sub-grid cell size) effects on the flow will be highly device-dependent. In this first case, the energy is assumed to be removed uniformly by a sub-grid scale array of devices from an area the size of one horizontal, computational cell (200 m in width by 200 m length by the total water depth), and calculations are based on depth-averaged velocities, after running the model in 3-D mode.

The effect of power extraction from the tidal flow is simulated by introducing a sink term into the governing momentum equations in the grid cell containing the presumed extraction devices. The derivation of this sink term (Defne et al. [18]) begins by defining a retarding force per unit area that is collinear with the direction of the flow as

{deviceforce}
$$\vec{F} = -\frac{p_{ext}}{|\vec{V}|} \cdot \frac{\vec{V}}{|\vec{V}|} \tag{2}$$

where $\vec{F}$ is the retarding force per unit surface area, $\vec{V}$ is the flow velocity vector, and p_{ext} is the extracted power density (power per unit cross-sectional area), given by

{Pextract}
$$p_{ext} = C_{ext} \cdot p \tag{3}$$

Here C_{ext} is the extraction coefficient and p is the local kinetic power density. Although Equation 3 makes it appear as an efficiency, the extraction coefficient does not have a simple physical interpretation or upper bound. At its lower bound of zero, no power is extracted; the device is transparent to the flow. As the extraction coefficient is increased, it tends to enhance extracted power, but the corresponding increase in drag force modifies the flow field and the local kinetic power. Scenario-specific transfers of potential to kinetic energy also occur. Thus the coefficient appearing before the kinetic power actually leads to dissipation of both kinetic and potential power. A typical hydropower reservoir represents an extreme example, where the kinetic energy of the reservoir fluid is negligible ($p \rightarrow 0$), but significant power is extracted after this energy is converted from potential to kinetic form. In this case, C_{ext} becomes infinite.

To obtain the sink terms that are substituted into the governing equations for the x and y directions, Equations 2 and 3 are combined to obtain

{Fu}
$$F_u = -C_{ext} \cdot \frac{1}{2} \cdot \rho \cdot u \cdot |\vec{V}| \tag{4}$$

and

{Fv}
$$F_v = -C_{ext} \cdot \frac{1}{2} \cdot \rho \cdot v \cdot |\vec{V}| \tag{5}$$

where ρ is the water density, u and v are the velocity components in the x and y directions, respectfully, so that $|\vec{V}| = \sqrt{u^2 + v^2}$, and F_u and F_v are the retarding force components per unit surface (bed) area. The retarding force was distributed over the water column in the three-dimensional flow model, but Equations 4 and 5 are presented here using depth-averaged quantities.

The total power dissipated (P_{diss}) from the flow field includes the power extracted as well as

any other losses and is found as

{Pdiss}
$$P_{diss} = p_{ext} \cdot dx \cdot dy \tag{6}$$

where dx and dy are the grid cell dimensions in the x and y (horizontal) directions, respectively.

The total available kinetic power within the channel cross-section is defined as

{Pkinetic}
$$P_{kinetic} = \sum_{i=1}^{I} \frac{1}{2} \cdot \rho \cdot |\vec{V}_i|^3 \cdot h_i \cdot w_i \tag{7}$$

where h_i, and w_i are the water depth and width of each cell across the channel, $|\vec{V}_i|$ is the depth-averaged velocity at each of these locations, and I is their total number.

The total available *potential* power within a channel cross-section is defined as

{Ppotential}
$$P_{potential} = \sum_{i=1}^{I} \rho \cdot g \cdot h_i \cdot |\vec{V}_i| \cdot \eta_i \cdot w_i \tag{8}$$

where g is the acceleration of gravity and η_i is the sea level fluctuation away from the mean water level. An estimate of the total power contained within a channel cross-section is simply the sum of the total available kinetic and potential energy given by

{Pavail}
$$P_{avail} = P_{kinetic} + P_{potential} \tag{9}$$

As noted, some of the potential power is converted to kinetic form as power is dissipated from the flow. The potential power is much greater than the kinetic, but is less readily harvested without a barrage.

The available kinetic power was evaluated for the instrumented site prior to installation of any energy extraction devices, based on time series generated from the harmonic constituents derived from the measurements. Available kinetic power was evaluated for each hour of a year,

and the resulting histograms of depth-averaged flow and power density are shown in Figure 6. The most likely depth-averaged flow speed is 70-75 cm/s for the site. The most likely kinetic power corresponds to the 0-45 W/m^2 band, which is simply a reflection of the fact that there are many hours within the 12-hour tidal cycle during which flows are mild.

The cumulative kinetic power available over a given time period is a more useful result and indicator of energy extraction viability. Integrating the model results over the water depth, across the channel, and over an entire month, yields, in this case, 610 MW-hrs per month.

Energy extraction effects were then simulated with the model via the use of Equations 2 through 6 applied at the velocity measurement site. A value of 0.2 was selected for the parameter C_{ext}, resulting in dissipation equivalent to 10% of the undisturbed total kinetic power of the flow in the full channel. The left panel of Figure 7 shows the influence of the energy extraction on the mean flow field. The energy extraction results in a noticeable reduction in flow speed at the extraction point, but an increase adjacent to this point. In a sense, the energy extraction acts similarly to an obstacle, forcing some of the flow to take another path, thereby increasing flow speed along that alternative path. It also enhances dissipation, and results in transfer of some energy from potential to kinetic form. The difference in this case is not large, however - the maximum increase in flow speed that is observed is only about 5 cm/s. Peak flow speeds at locations A and B landward and seaward of the extraction point (Figure 7) are reduced by 10 cm/s.

The right panel of Figure 7 provides a similar comparison for water levels, again for the 10% energy extraction target. Maximum water level differences are about 10 cm (approximately 5% of range) at both locations A and B, occurring near low tide. The energy extraction introduces a slight phase lag in the velocity time series. Karsten et al. [11] noted that the phase shift induced by energy extraction can actually increase the tide range by pushing the basin closer to resonance, but this effect is not observed here.

The kinetic power in the flow both with and without the 10% energy extraction scenario is shown in Figure 8, along with the dissipated power. The dissipated power reaches a maximum

of 0.31 MW, and integrating this term over the entire record gives a total of 62.8 MW-hrs/month, roughly 10% of the total 610 MW-hrs/month available in the flow. The dissipated power represents all energy losses, so is larger than the power that would be extracted by an energy harvesting system.

The extraction coefficient C_{ext} in Equation 3 was then changed to simulate a scenario where 60% of the initially available kinetic power in the channel is dissipated. The single cell considered earlier does not contain enough kinetic power to allow extraction of the full 60% of the kinetic power in the channel, so the harvesting area was doubled to two cells, and the extraction coefficient reduced to 0.05. Despite the lower coefficient, the larger footprint of the harvesting area results in significantly larger dissipated power. The fact that the extraction coefficient was reduced while dissipated power increased six-fold emphasizes the point that the extraction coefficient is not simply an efficiency and has a complicated, nonlinear relationship on the dissipated power.

Results are shown in Figures 9 and 10. Qualitatively, the results look similar to the 10% dissipated power simulation, but differences are amplified. Peak flow speeds are reduced by 10 cm/s at the extraction site, and increased by a lesser amount across the rest of the flow cross-section there. Maximum water level is reduced by up to 8 mm landward, with less significant increases seaward. Small changes appear in the channel connecting the Beaufort and Broad Rivers along the northern boundary of Parris Island, revealing the fact that aggressive energy harvesting has the potential to change circulation patterns in an estuary. In this case, however, the changes are small in both magnitude and spatial extent.

Power with and without energy harvesting for this 60% extraction case is shown in Figure 11. Peak dissipated power increases to 1.59 MW, totalling 371 MW-hrs per month, or 61% of the 610 MW-hrs/month of kinetic energy available in the undisturbed flow. The dissipated kinetic power is actually greater than the difference between the undisturbed kinetic power and the residual kinetic power, highlighting the conversion of potential to kinetic power that occurs.

5. Velocity Profile Considerations

As noted earlier, there are many factors governing site suitability beyond the magnitude of the available power and the flow field changes induced by energy extraction. Many previously reported site investigations or methodologies have made use of either one-dimensional or 2DH (i.e. depth-averaged) flow models which do not resolve vertical gradients in horizontal velocity in the flow. The importance of the three-dimensionality of the flow increases for a shallower site such as that considered here, because for a given device size, it is more difficult to avoid strong variations in flow speed across the energy extraction area.

Bryden et al. [31] suggested the calculation of a representative velocity when computing potential power, accounting for flow speed variations over the vertical to arrive at a more realistic description of the available power. Here a correction to their approach is made, and time-dependence in both the depth and velocity addressed. Note also that the goal here is to identify, to first order, a device-independent, optimal altitude for the tidal energy converter, rather than the actual power extracted. For this, the pre-installation, incident power is considered.

A circular harvesting area of diameter D is assumed, with sinusoidal velocity at the water surface: $u_s = u_o \sin \omega t$. A 1/7th-power velocity profile is also assumed (Streeter and Wylie [32]; Bryden et al. [31]) to simulate variation in horizontal velocity with altitude above a turbulent boundary layer. Actually the method employed here could similarly be applied using a logarithmic velocity profile (e.g. Vanoni [33]), or in fact any other form of analytical or measured velocity profile, or any harvesting area geometry, via the use of numerical integration.

The instantaneous mean velocity over the swept area is then

{umean}
$$\overline{u}(t) = \frac{4}{\pi D^2} \int_{-D/2}^{D/2} u_s \left(\frac{z_o + y}{h} \right)^{1/7} D \sin \left[\cos^{-1} \left(\frac{2y}{D} \right) \right] dy \tag{10}$$

where u_s and h are the instantaneous, time-dependent surface velocity and total water depth, respectively. Altitude of the center of the harvesting area above the channel bottom is denoted

by z_o, and y is the vertical coordinate relative to this center (Figure 12). It is assumed that the entire harvesting area must remain submerged, and above the bottom, so it is required that $\frac{D}{2} < z_o < h_o - \frac{D}{2}$, where h_0 is the water depth at low tide.

The corresponding instantaneous, representative, incident velocity u_r, assuming that power varies as the cube of flow speed, is

{urep}
$$u_r(t) = \left[\overline{u^3}\right]^{1/3} = \left[\frac{4}{\pi D^2}\int_{-D/2}^{D/2} u_s^3 \left(\frac{z_o + y}{h}\right)^{3/7} D \sin\left[\cos^{-1}\left(\frac{2y}{D}\right)\right] dy\right]^{1/3} \quad (11)$$

The instantaneous, incident, kinetic power may then be estimated as $P(t) = \frac{1}{2}\rho A u_r^3(t)$, where A is the swept area and ρ is water density. The time-averaged power may be evaluated as

{meanP}
$$\overline{P} = \frac{1}{T}\int_t^{t+T} P(t)dt \quad (12)$$

where T denotes the period associated with the flow, or 12.42 hours for a tidally forced flow dominated by the M2 harmonic constituent.

If the surface flow speed is assumed sinusoidal in time, mean power may be expressed as

{meanP2}
$$\overline{P} = \frac{1}{T}\int_t^{t+T} \frac{1}{2}\rho u_o^3 \left|sin^3 \omega t\right| \left[\int_{-D/2}^{D/2} \left(\frac{z_o + y}{h}\right)^{3/7} D \sin\left[\cos^{-1}\left(\frac{2y}{D}\right)\right] dy\right] dt \quad (13)$$

assuming that power is produced during the full bidirectional flow cycle. In evaluating Equation 13 for the example appearing here, water depth h was also taken as a harmonic quantity, assumed ninety degrees out-of-phase with the velocity. In practice, this phase difference can vary with both location and time. If the tide range is much smaller than the depth, the depth in Equation 13 can simply be taken as the mean water depth at the site.

The incident power varies with altitude z_o and diameter D of the harvesting area, and the diameter is constrained by the proximity of the device to the water surface or seabed. Figure 13 shows this depth dependence for two cases. If the harvesting area is made as large as possible for a given altitude, to where it just touches the low tide water surface or the seafloor, the variation in incident power with depth is shown by the solid line. In this case, maximum incident power occurs with the center of the area at mid-depth, which allows for the largest possible diameter (equal to the water depth), and then power decreases quickly as altitude is increased or decreased, since this requires a decrease in harvesting area. The curve is not symmetric about the mean depth, however, since the flow speeds are smaller near the bottom of the water column.

The dashed line in Figure 13 shows the result if the size of the harvesting area is constrained (in this case, to a maximum diameter of 4 m, or half of the water depth). In this case the altitude of the point that maximizes the power potential is greater (although the peak power by which the curve is non-dimensionalized is reduced, due to the smaller maximum area). The curve has three discontinuities. Two correspond to the points where distance from a boundary is just sufficient to allow the use of the chosen maximum area, and the third corresponds to the ideal location, from a power production perspective, given the constraint on area. Although a bit simplified because of the sinusoidal velocity and depth assumptions, this approach could also be used with a measured or modeled velocity profile to estimate the fraction of power sacrificed by moving the turbine up or down in the water column to accomodate logistical constraints. This approach is suitable for an intial feasibility investigation; for final design, a more sophisticated approach is recommended that describes near-field modifications to the flow field arising from the presence of the harvesting device.

The vertical variation in velocity also plays an important role in the drag force on the tidal energy converter. Large variations in horizontal flow speed across the device's swept area can result in undesirable forces on internal bearings. A simple measure of the significance of this variation would be $\Delta u^2/u^2$ where Δu^2 defines the maximum range in the square of the velocity

of the swept area and u^2 is the square of the velocity at the center or the representative velocity defined above. If the site is also exposed to wind waves, the additional velocity and acceleration corresponding to the wave-induced flow should be considered as well, since this will enhance the force on the device and support structure, and these wave-induced forces also vary with depth.

6. Summary and Conclusions

Although few operational projects have been constructed to date, many site investigations have been performed to define the potential for generation of renewable energy via tidal energy conversion devices, or their impacts on the environment. The level of complexity in these investigations varies widely, reflecting the fact that sites with the greatest potential are scattered across the globe and as a result there is no single entity regulating the development of the resource. The field is also new enough that standards for site assessment are still evolving.

Some early site assessments were based primarily on tidal range or observed or predicted flow speeds. Subsequent investigations have included one-dimensional, analytical or numerical simulations of tidal flows. One-dimensional flow through branching channels represents one step up from this approach in terms of model sophistication. Other studies have included 2DH (two dimensions in the horizontal plane), or three-dimensional simulations, as here. Ideally, one would employ at least a 2DH approach, which allows simulation of the effects of the deployed energy extraction device(s) on the surrounding flow field. As shown here, the tidal power device can act similarly to an obstacle to the flow, reducing flow speed nearby, and enhancing it elsewhere.

The site considered in this investigation is a tidal river with negligible freshwater inputs in coastal South Carolina, in the southeastern United States. Other than the work done by the authors (e.g. Defne et al. [18]), no prior assessments of tidal power potential within the region have been published. This is in part because at a bit over 2 m, the tidal range is not particularly large, but the site considered here features one of the largest ranges in the region, and corresponding (relatively) large tidal currents, with negligible mean flow.

394 The number of previous studies that specifically included field measurements to quantify power
395 potential or validate model results is surprisingly small; some prior efforts have essentially in-
396 cluded no validation of the computed velocities. The effort described here included both field mea-
397 surement and numerical modeling phases. Field measurements included a survey of bathymetry
398 within the target area, measurement of the flow field during maximum ebb and flood portions of
399 one tidal cycle, and deployment of a bottom-mounted acoustic Doppler current profiler (ADCP)
400 on the riverbed at a location with relatively large tidal currents for 37 days, to provide data for
401 a period exceeding a lunar month so that harmonic constituents of the water level and velocity
402 time series could be computed. Model performance was good for both water level and velocity;
403 the maximum difference between measurements and model results in any of the four primary tidal
404 constituents was 7 cm for water level and 9 cm/s for velocity. These values correspond to 3 percent
405 of the mean tidal range of 2.3 m and 9 percent of the peak measured flow speed, respectively.

406 The model used here yielded time-dependent, three-dimensional velocity fields that were used
407 to quantify power potential within one or two computational cells where a power generation system
408 might be deployed. The system was simulated by the introduction of an additional drag force at
409 the point of interest, modeling the removal of 10-60% of the kinetic power from the channel cross-
410 section, based on pre-development values. With the smaller level of power dissipation, the flow
411 is diverted laterally away from the dissipation point, similar to what would occur if an obstacle
412 were introduced there. Flow speed near the dissipation site was reduced roughly 20%, with an
413 increase of five percent at the adjacent location. Water levels upstream were reduced because of
414 the dissipation, but not measurably - only 1-2 mm change was predicted. Qualitatively, results
415 were very similar when dissipation of 60% of the undisturbed kinetic power across the channel
416 was simulated, but the magnitude of the change was enhanced slightly. Water levels landward were
417 modified by up to half a centimeter, and some changes in the channel connecting the Beaufort and
418 Broad Rivers became evident, highlighting the fact that the installation of a small (meters) energy
419 extraction device can result in changes in circulation patterns at much larger scales (1-10 km).

Many southeastern U.S. estuaries and rivers feature relatively shallow depths. For example, the site considered here features depths < 10 m. Shallow water presents several logistical challenges and an optimization problem. Typically it would be desirable to avoid small clearances between the swept area of an energy conversion device and the seabed or the water surface - the former to help avoid scour and the latter to avoid interference with vessels. But flow speed increases with altitude above the lower boundary of the flow. A methodology was presented to quantify this tradeoff to reveal an estimate of the percentage of the potential power that is sacrificed by moving the energy extraction device vertically upward or downward within the water column. If the only constraint is to keep the harvesting area submerged, the optimal location is halfway between the low water level and the seabed, with the harvesting area spanning the full water column. But if a more restrictive upper bound is placed on harvesting area, the optimal location moves upward to take advantage of the greater flow speed there.

The methods by which a site's potential for production of renewable energy from tidal currents is quantified are still evolving. Because of the complicated, nonlinear influence of power dissipation on the flow field, a three-dimensional hydrodynamic model is the most suitable tool. Consideration of the three-dimensionality of the flow is important to optimize the vertical location for energy extraction and to predict forces on the deployed equipment. Whatever method is employed, it is recommended that model results be compared to field measurements for model calibration and validation. It is particularly important to have velocity measurements, as predicted velocities typically contain greater uncertainty than water levels, and power varies strongly with velocity.

7. Acknowledgements

This work was supported by the U.S. Marine Corps, whose support is gratefully acknowledged. Trent Moore from the Skidaway Institute of Oceanography (Savannah, Georgia, USA) assisted with the field component of the project.

References

[1] Bryden, I., Melville, G.. Choosing and evaluating sites for tidal current development. Proc of the Inst of Mech Eng, Part A: J of Power and Energy 2004;218:567–577.

[2] Blanchfield, J., Garrett, C., Wild, P., Rowe, A.. The extractable power from a channel linking a bay to the open ocean. Proc Inst of Mech Eng Part A: J of Power and Energy 2008;222:289–297.

[3] Garrett, C., Cummins, P.. The efficiency of a turbine in a tidal channel. J Fluid Mech 2007;588:243–251.

[4] Atwater, J., Lawrence, G.. Power potential of a split tidal channel. Renewable Energy 2010;35:329–332.

[5] Polagye, B., Malte, P.. Far-field dynamics of tidal energy extraction in channel networks. Renewable Energy 2011;36:222–234.

[6] Alnaser, W.. Estimation of energy from tide, wave and sea water currents in Bahrain. Renewable Energy 1993;3(2/3):235–238.

[7] Blunden, L., Bahaj, A.. Initial evaluation of tidal stream energy resources at Portland Bill, UK. Renewable Energy 2006;31:121–132.

[8] Brooks, D.. The tidal-stream energy resource in Passamaquoddy-Cobscook Bays: A fresh look at an old story. Renewable Energy 2006;31:2284–2295.

[9] Sutherland, G., Foreman, M., Garrett, C.. Tidal current energy assessment for Johnstone Strait, Vancouver Island. Proc Inst of Mech Eng Part A: J of Power and Energy 2007;221:147–157.

[10] Blanchfield, J., Garrett, C., Rowe, A., Wild, P.. Tidal stream power resource assessment for Masset Sound, Haida Gwaii. Proc Inst of Mech Eng Part A: J of Power and Energy 2008;222:485–492.

[11] Karsten, R., McMillan, J., Lickley, M., Haynes, R.. Assessment of tidal current energy in the Minas Passage, Bay of Fundy. Proc of the Inst of Mech Eng Part A: J of Power and Energy 2008;222:493–507.

[12] Polagye, B., Kawase, M., Malte, P.. In-stream tidal energy potential of Puget Sound, Washington. Proc Inst of Mech Eng Part A: J of Power and Energy 2009;223:571–587.

[13] Carballo, R., Iglesias, G., Castro, A.. Numerical model evaluation of tidal stream energy resources in the Ria de Muros (NW Spain). Renewable Energy 2009;34:1517–1524.

[14] Tontolo, H., Duvoy, P., Vanlesberg, S., Johnson, J.. Modelling and field measurements in support of the hydrokinetic resource assessment for the Tanana River at Nenana, Alaska. Proc Inst of Mech Eng Part A: J of Power and Energy 2010;224:1127–1139.

[15] Xia, J., Falconer, R., Lin, B.. Numerical model assessment of tidal stream energy resources in the Severn Estuary, UK. Proc Inst of Mech Eng Part A: J of Power and Energy 2010;224:969–983.

[16] Brooks, D.. The hydrokinetic power resource in a tidal estuary: the Kennebec River of the central Maine coast.

476 Renewable Energy 2011;36:1492–1501.
477 [17] Defne, Z., Haas, K., Fritz, H.. GIS based multi-criteria assessment of tidal stream power potential: A case
478 study for Georgia, USA. Renewable and Sustainable Energy Reviews 2011;15:2310–21.
479 [18] Defne, Z., Haas, K., Fritz, H.. Numerical modeling of tidal currents and the effects of power extraction on
480 estuarine hydrodynamics along the Georgia coast, USA. Renewable Energy 2011;37:3461–3471.
481 [19] Couch, S., Bryden, I.G.. Tidal current energy extraction: hydrodynamic resource characteristics. Proc of the
482 Inst of Mech Eng, Part M: J of Engineering for the Maritime Environment 2006;220(4):185–194.
483 [20] Garrett, C., Cummins, P.. Limits to tidal current power. Renewable Energy 2008;33:2485–2490.
484 [21] Vennell, R.. Estimating the power potential of tidal currents and the impact of power extraction on flow speeds.
485 Renewable Energy 2011;36:3558–3565.
486 [22] Neill, S., Litt, E., Couch, S., Davies, A.. The impact of tidal stream turbines on large-scale sediment dynamics.
487 Renewable Energy 2009;34:2803–2812.
488 [23] Neill, S., Jordan, J., Couch, S.. Impact of tidal energy converter (TEC) arrays on the dynamics of headland
489 sand banks. Renewable Energy 2012;37:387–397.
490 [24] Pawlowicz, R., Beardsley, B., Lentz, S.. Classical tidal harmonic analysis including error estimates in MAT-
491 LAB using T-TIDE. Computers and Geosciences 2002;28:929–937.
492 [25] Haidvogel, D., Arango, H., Budgell, W., Cornuelle, B., Curchitser, E., Di Lorenzo, E., et al. Regional
493 ocean forecasting in terrain-following coordinates: model formulation and skill assessment. J of Computational
494 Physics 2008;227(7):3595–3624.
495 [26] Shchepetkin, A., McWilliams, J.. The Regional Ocean Modeling System (ROMS): A split-explicit, free-
496 surface, topography following coordinates ocean model. Ocean Modeling 2005;9:347–404.
497 [27] Mukai, A., Westerink, J., Luettich, R., Mark, D.. Eastcoast 2001, a tidal constituent database for western
498 North Atlantic, Gulf of Mexico, and Caribbean Sea. 2002.
499 [28] Hagerman, G., Polagye, B., Bedard, R., Previsic, M.. Methodology for estimating tidal current energy
500 resources and power production by tidal in-stream energy conversion (TISEC) devices. EPRI-TP-001 NA Rev
501 3. Electric Power Research Institute; 2006.
502 [29] Polagye, B., Malte, P., Kawase, M., Durran, D.. Effect of large-scale kinetic power extraction on time-
503 dependent estuaries. Proc Inst of Mech Eng Part A: J of Power and Energy 2008;222:471–484.
504 [30] Garrett, C., Cummins, P.. Generating power from tidal currents. J of Waterway, Port, Coastal and Ocean Eng
505 2004;130:114–118.
506 [31] Bryden, I., Couch, S., Owen, A., Melville, G.. Tidal current resource assessment. Proc of the Inst of Mech

Eng Part A: J of Power and Energy 2007;221:125–135.

[32] Streeter, V., Wylie, E.. Fluid mechanics. New York: McGraw-Hill, Inc.; 8th ed.; 1985.

[33] Vanoni, V.. Velocity distribution in open channels. Civil Eng 1941;11:356–357.

Table 1: Harmonic analysis results derived from 37-day record of measured water levels and mean flows.

Constituent	**Period (hrs)**	**Water Level Amplitude (m)**	**Velocity Amplitude (m/s)**
M2	12.42	0.86	0.87
N2	12.66	0.19	0.18
K1	23.92	0.12	0.07
S2	12.00	0.11	0.11
MM	27.55 days	0.11	0.01
O1	25.84	0.06	0.04
L2	12.20	0.05	0.08
M4	6.21	0.05	0.06
M6	4.14	0.03	0.06

Table 2: Harmonic analysis results derived from ROMS simulation ("modeled") and 37-day record of water levels and mean flows ("measured").

Constituent	**Period (hrs)**	**Water Level (m)**		**Velocity Amp (m/s)**	
		Modeled	**Measured**	**Modeled**	**Measured**
M2	12.42	0.93	0.86	0.78	0.87
N2	12.66	0.20	0.19	0.16	0.18
K1	23.92	0.11	0.12	0.05	0.06
S2	12.00	0.12	0.11	0.10	0.11

Figure 1: Site location, model domain, and bathymetry. Black box in left image shows area of primary interest, roughly 1 km x 1.5 km. Right image shows numerical model domain and bathymetry. White box denotes area shown at left.

Figure 2: Measured, depth-averaged velocity magnitude during ebb tidal portion of survey. Acquired 18:15-20:51 GMT, 22 Oct 2009.

Figure 3: Measured water levels (top) and flow speeds (bottom) vs. time series reconstructed based on harmonic analysis constituents, with difference shown. Mean value of magnitude of difference in water level is 0.1 m, and 5 cm/s for flow speed.

Figure 4: Vertical variation of mean velocity based on data from bottom-mounted, up-looking ADCP. Zero depth corresponds to mean water level. Ebb and flood curves each represent mean of the mean flow for each three-hour window that includes the peak flow; the time-averaged curve represents the mean magnitude for the entire measurement period (37 days).

Figure 5: Mean (left panel) and maximum (right panel) flow speeds predicted by ROMS model for Nov 12 - Dec 17, 2009 period. Black box shows primary area of interest for energy extraction. Shade indicates velocity magnitude in m/s.

Figure 6: Histograms of depth-averaged flow speed and power density at ADCP measurement location.

Figure 7: Influence of 10% kinetic power extraction on mean flow speeds (left) and maximum water levels.

Figure 8: Time series of kinetic tidal current power contained in channel cross-section for the undisturbed flow case and the case with 10% kinetic power extraction.

Figure 9: Influence of 60% kinetic power extraction on flow speeds (left) and maximum water levels (right).

Figure 10: Time series of velocity magnitude for 60% energy extraction scenario for locations A (top) and B (bottom) shown in Figure 9.

Figure 11: Time series of kinetic tidal current power contained in channel cross-section for the undisturbed flow case and the case with 60% kinetic power extraction.

Figure 12: Geometry of tidal energy conversion device with circular swept area. End view (left) and profile view (right).

Figure 13: Variation in incident power with altitude of turbine hub. Solid line corresponds to case with diameter of turbine assumed as large as possible for any given hub altitude z_0. Dashed line assumes that turbine diameter is limited to less than half of the low-tide water depth h_0. Maximum power differs for the two cases; h_0 = 8 m for this example.

Figure1

Click here to download high resolution image

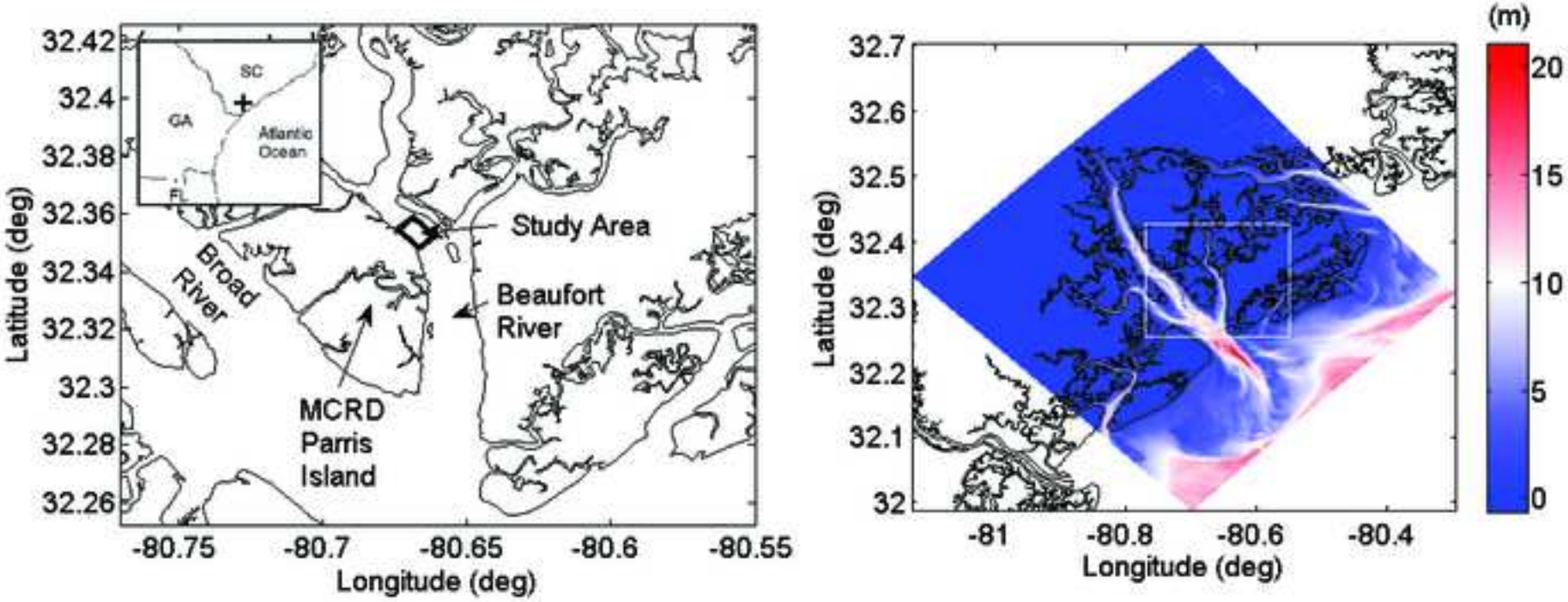

Figure2

Click here to download high resolution image

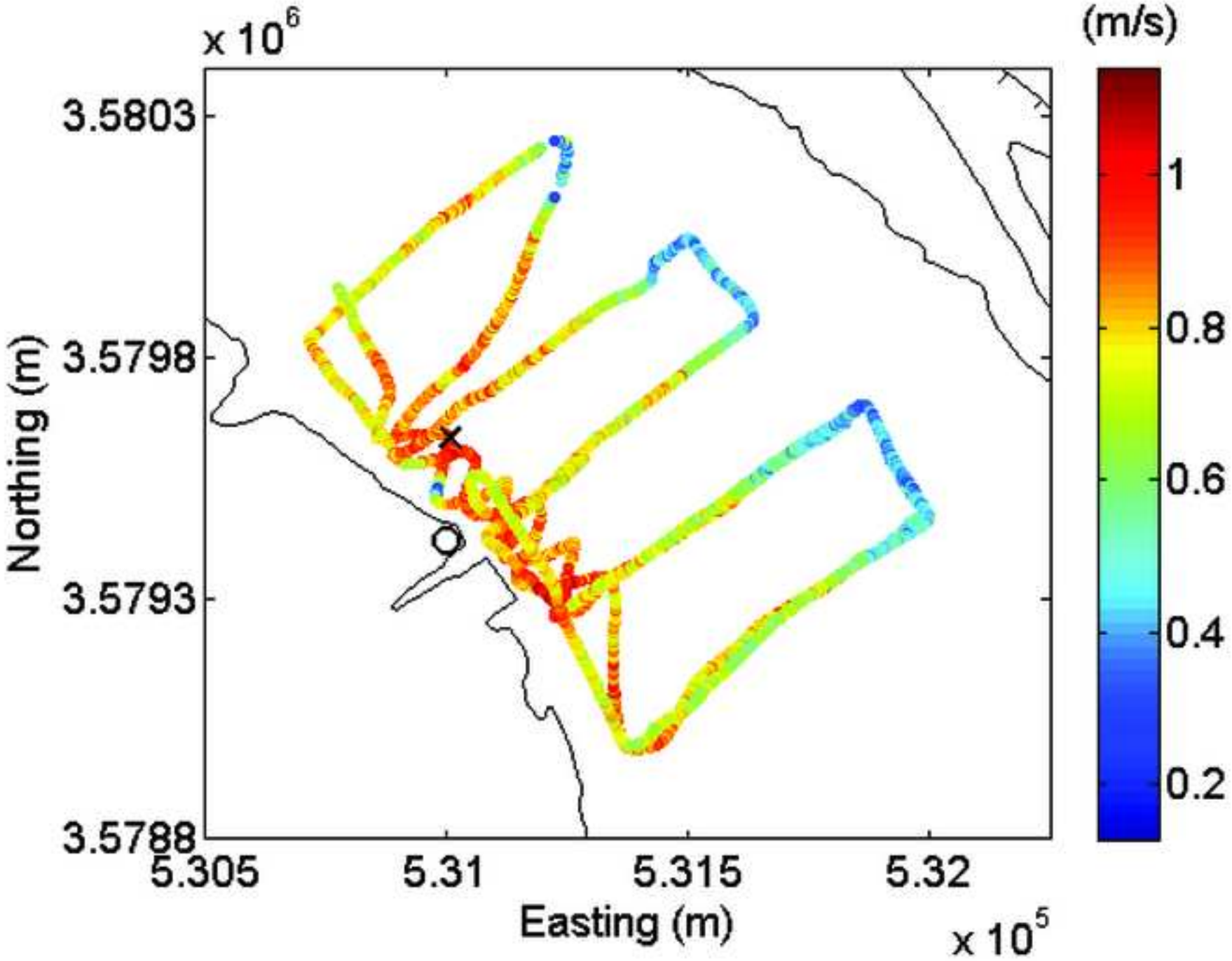

Figure3

Click here to download high resolution image

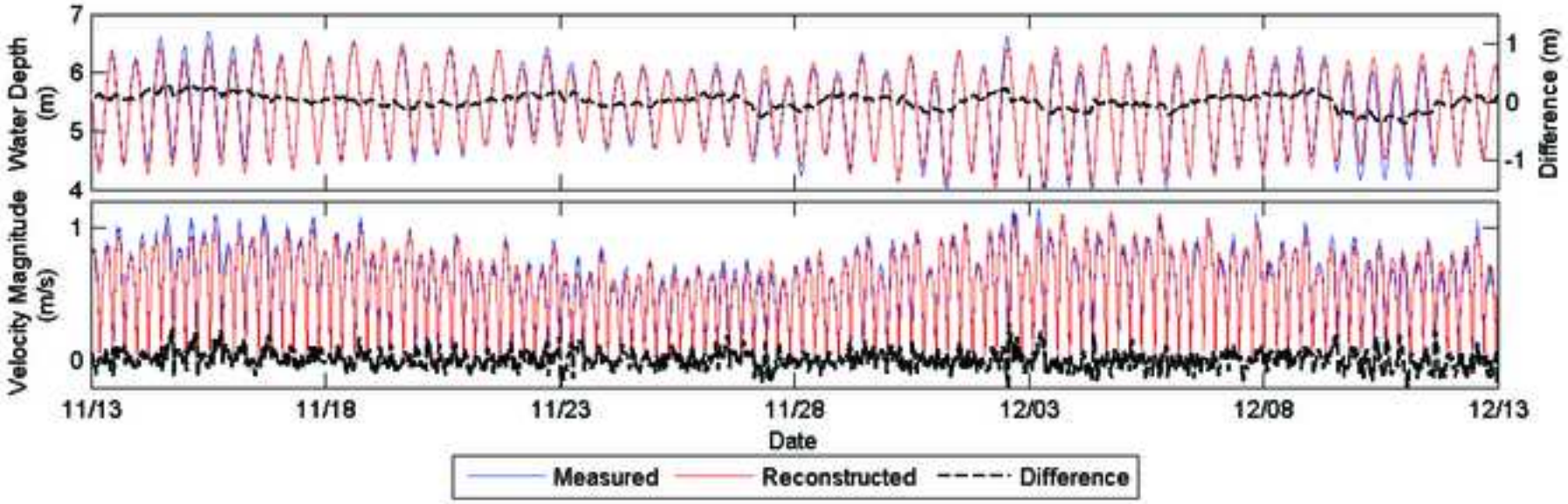

Figure4
Click here to download high resolution image

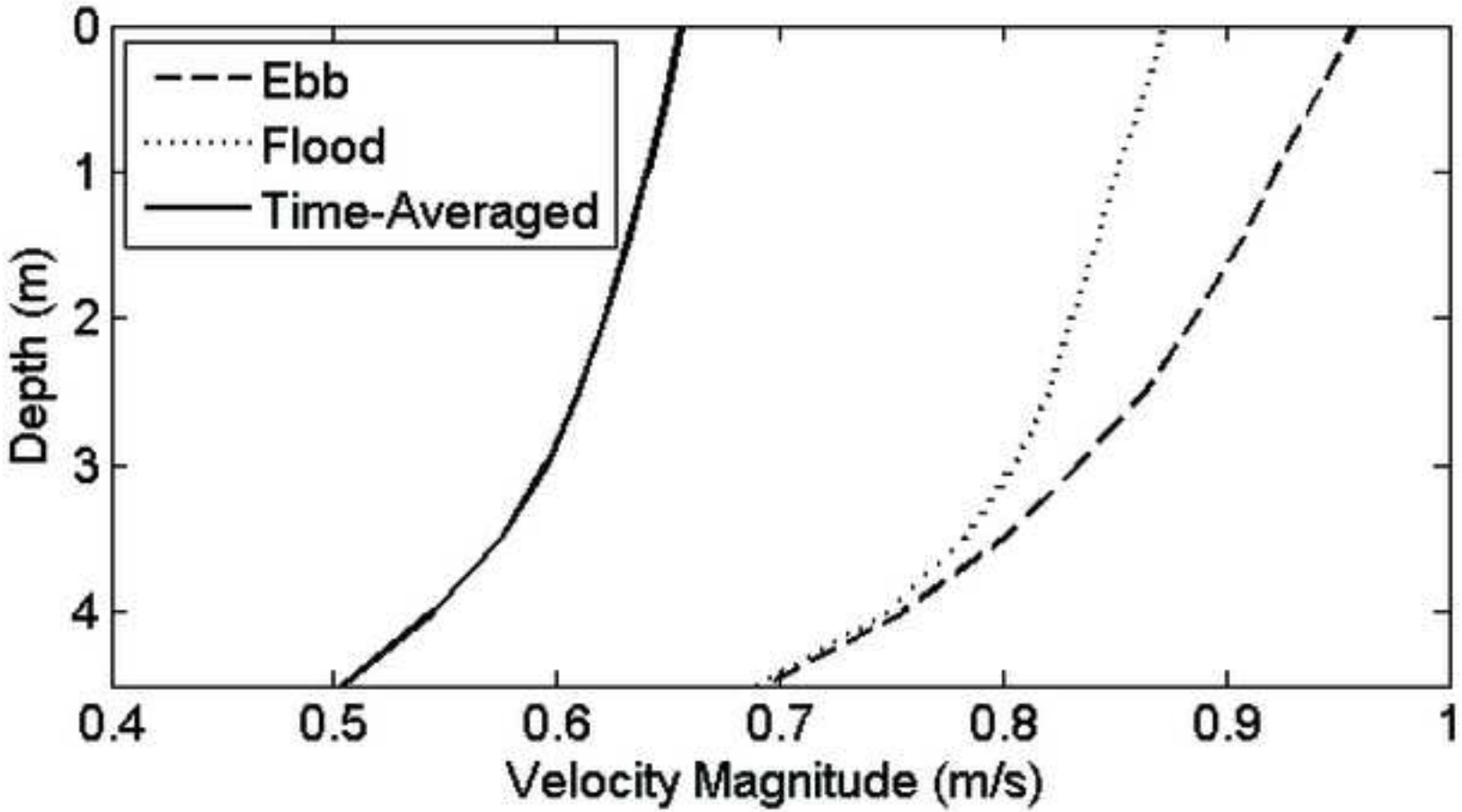

Figure5

Click here to download high resolution image

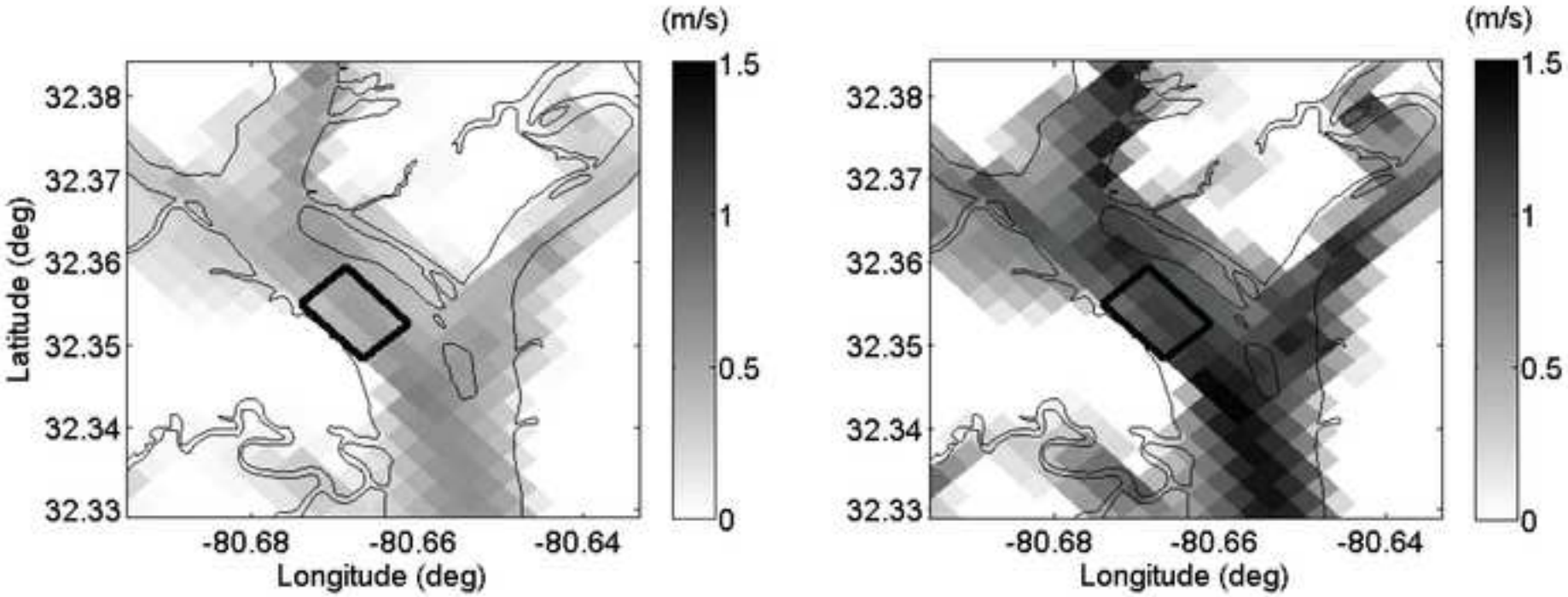

Figure6
Click here to download high resolution image

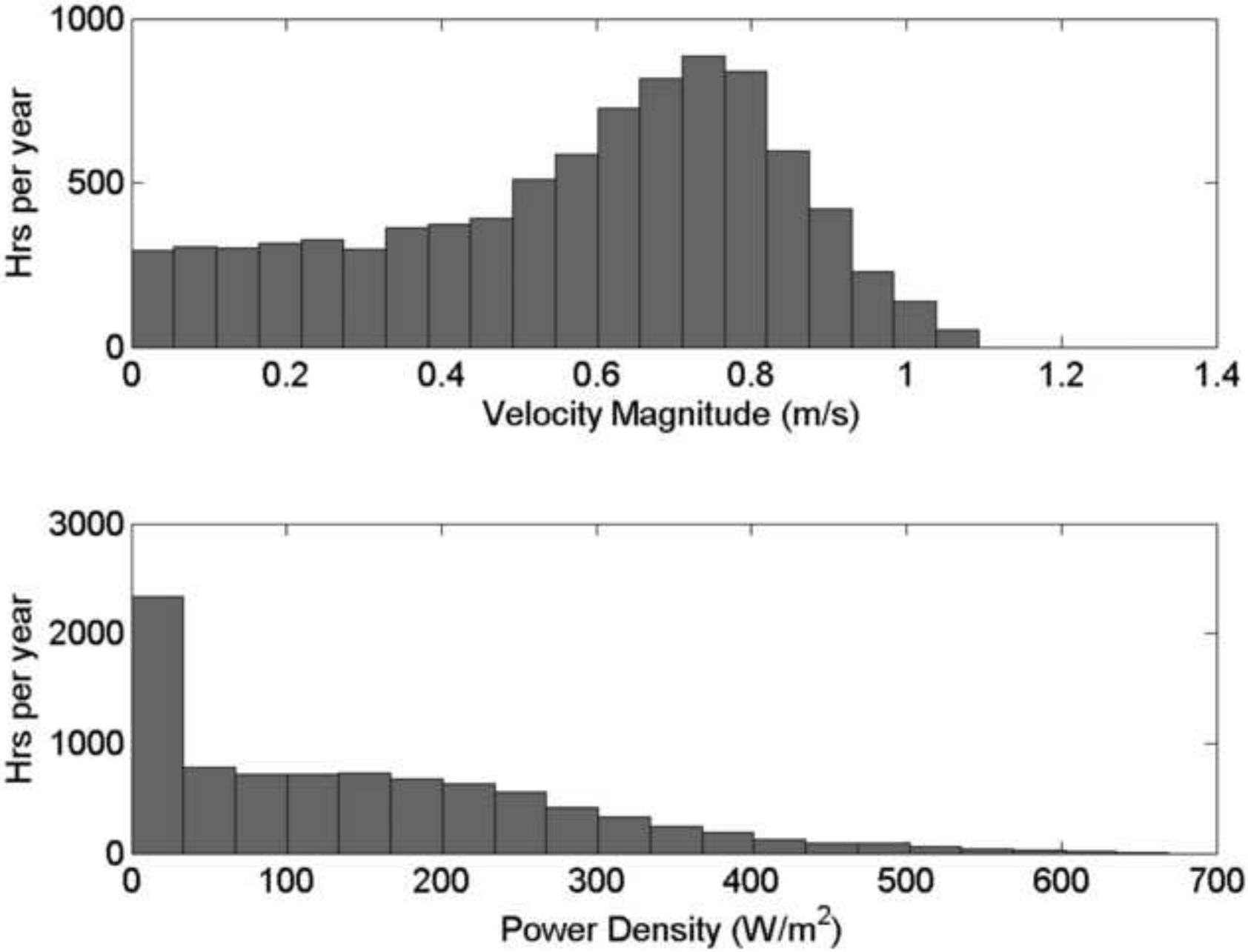

Figure7

Click here to download high resolution image

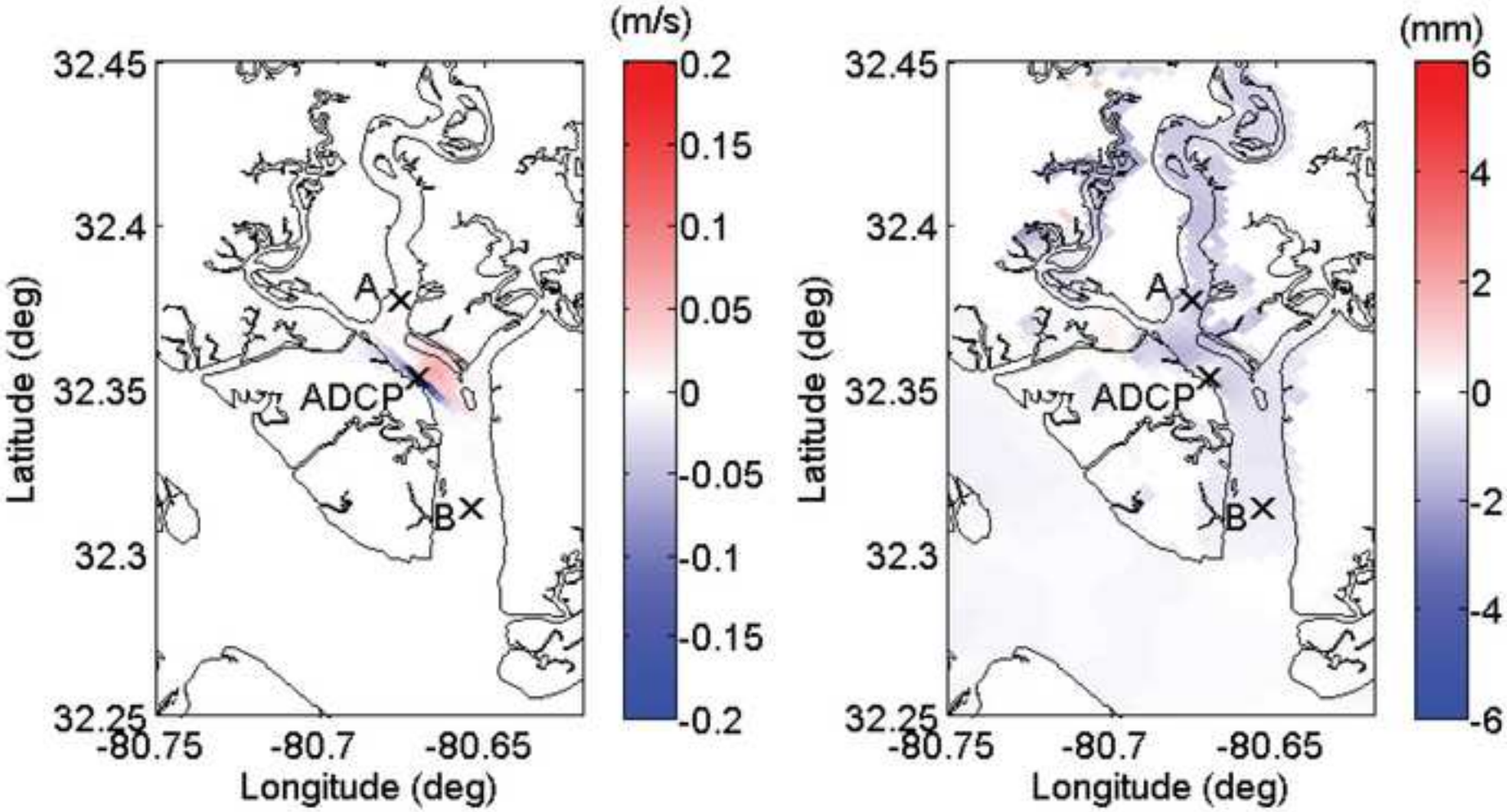

Figure8

Click here to download high resolution image

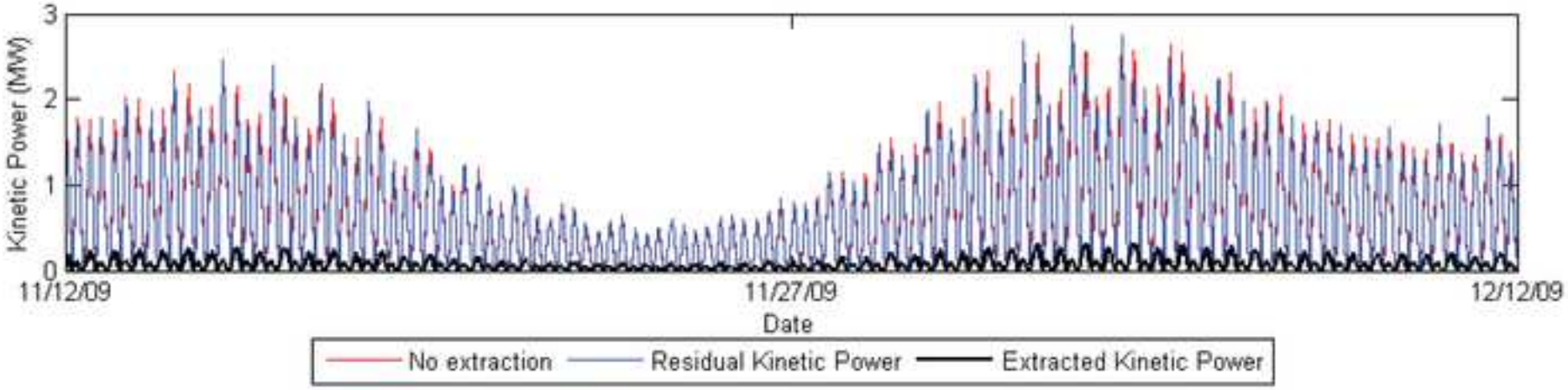

Figure9

Click here to download high resolution image

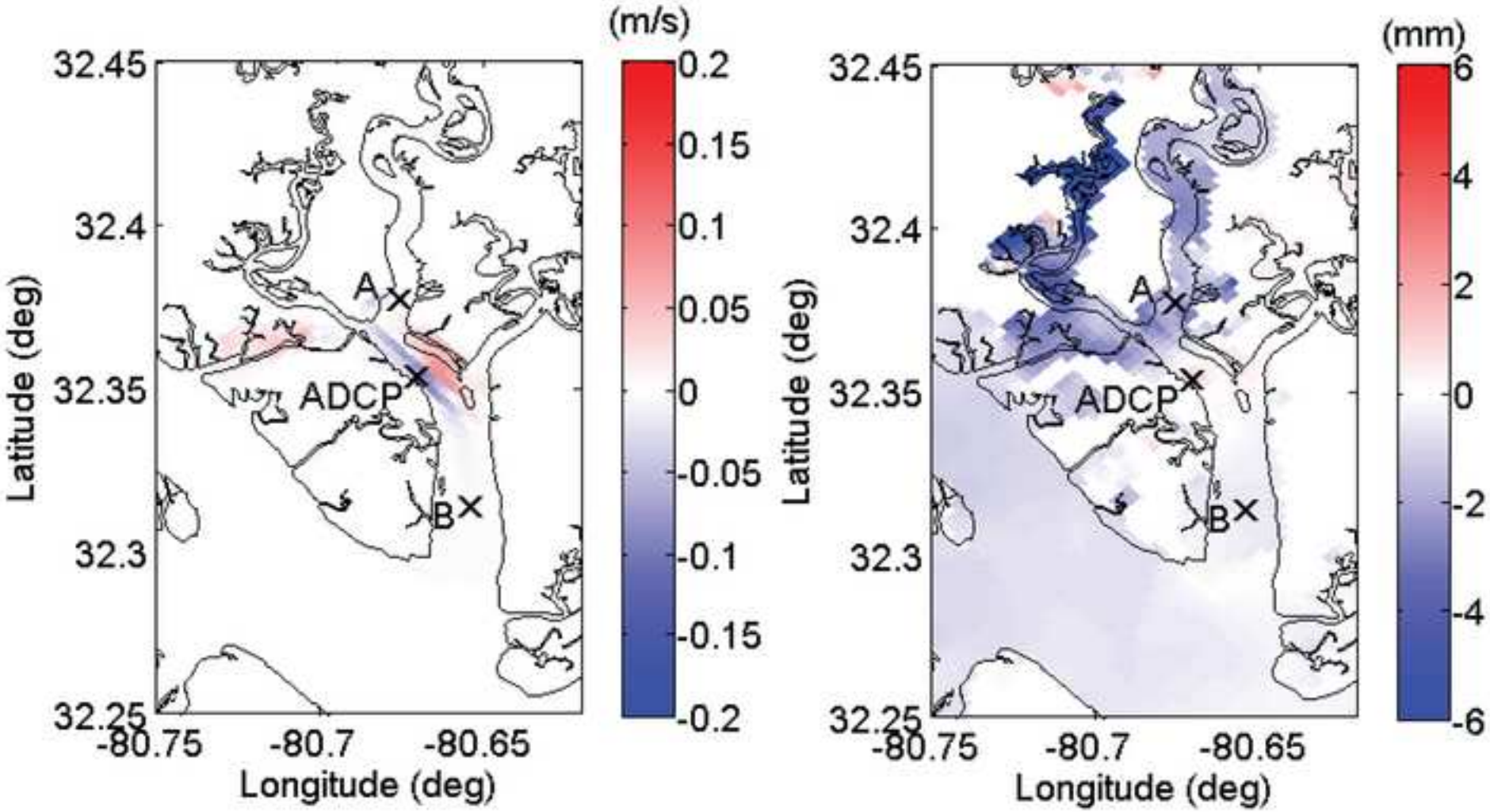

Figure10

Click here to download high resolution image

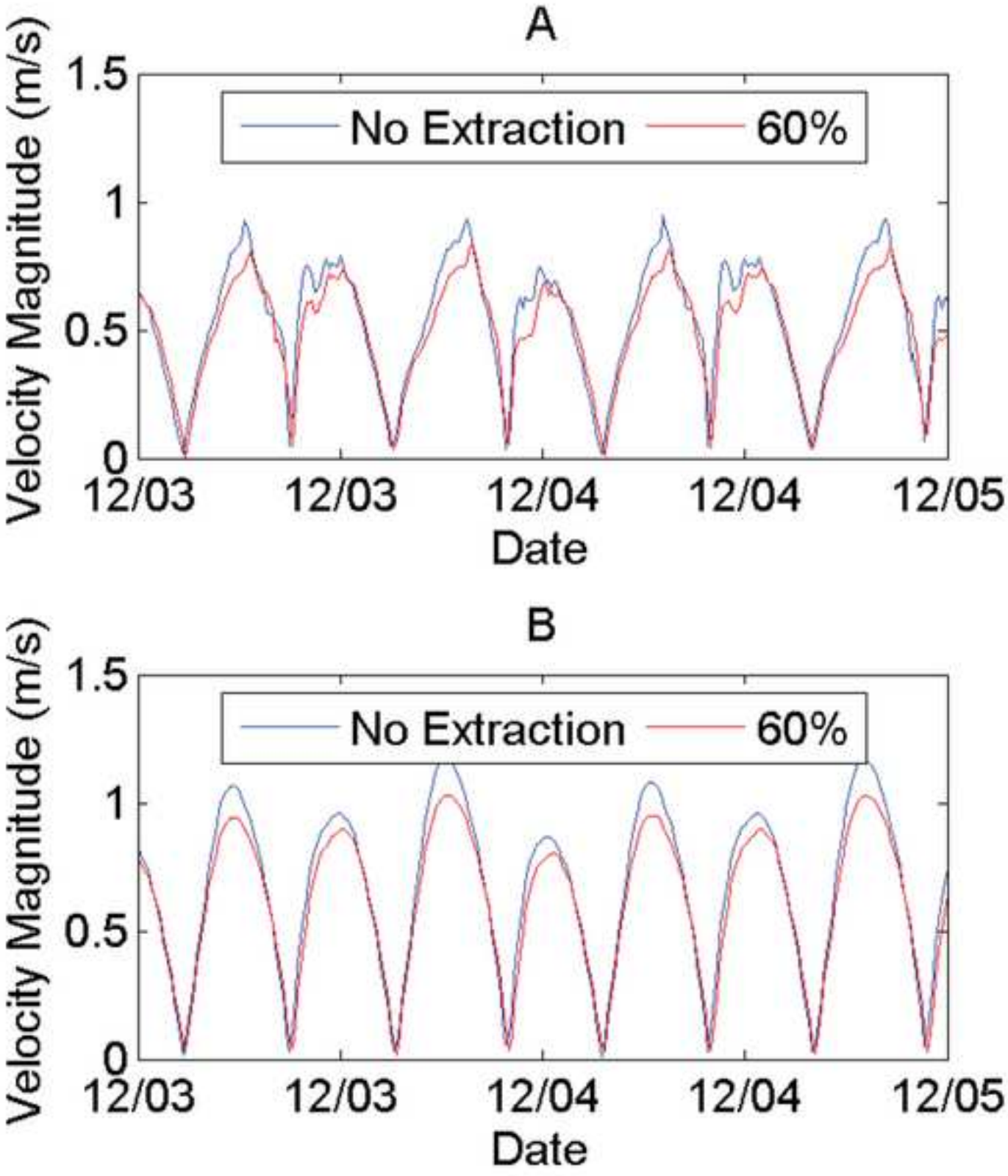

Figure11

Click here to download high resolution image

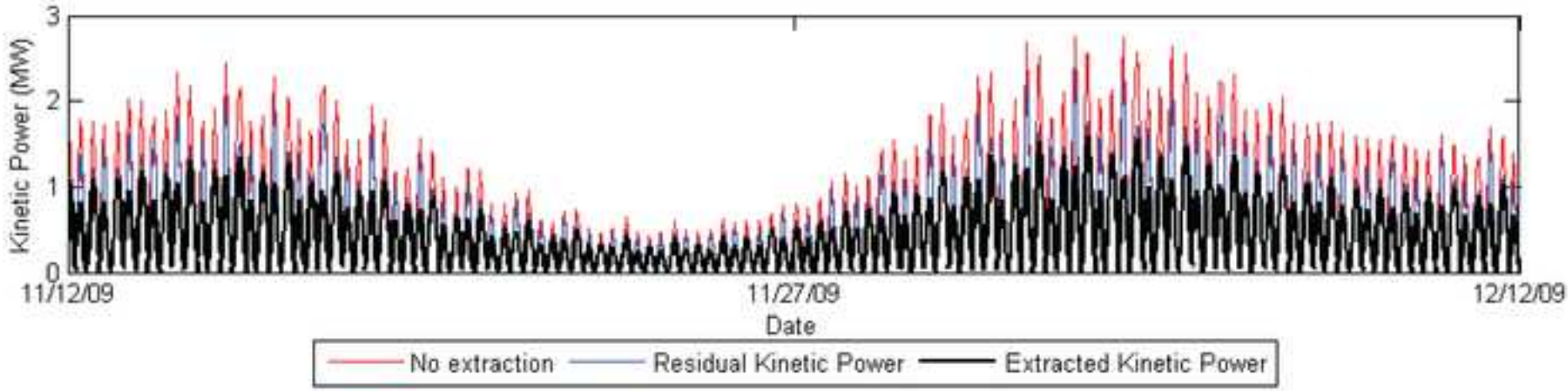

Figure12
Click here to download high resolution image

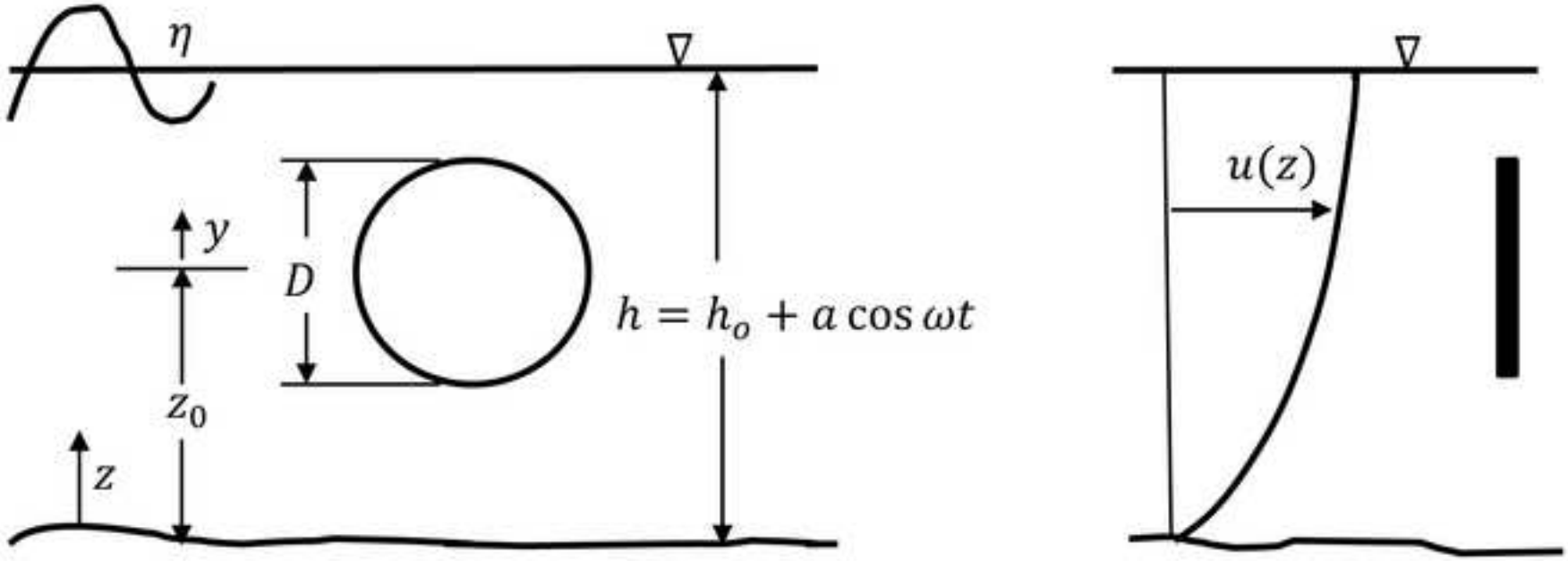

Figure13

Click here to download high resolution image